Journal of Materials Chemistry A

Bandgap-Adjustment and Enhanced Surface Photovoltage in Y-Substituted LaTa^{IV}O$_2$N

Journal Name

ARTICLE

Bandgap-Adjustment and Enhanced Surface Photovoltage in Y-Substituted LaTa^{IV}O$_2$N

Cora Bubeck[a,b], Marc Widenmeyer[a,**], Alexandra T. De Denko[c], Gunther Richter[d], Mauro Coduri[e,f], Eduardo Salas Colera[e,g], Eberhard Goering[h], Hongbin Zhang[i], Songhak Yoon[j], Frank E. Osterloh[c], Anke Weidenkaff[a,*]

Perovskite-type oxynitrides AB(O,N)$_3$ are photocatalysts for overall water splitting under visible light illumination. In the past, structurally labile perovskite-type oxynitrides (*e.g.* YTaON$_2$) were predicted to be highly suitable. In this work, we tackle the challenging YTa(O,N)$_3$ synthesis by Y-substitution in LaTa^{IV}O$_2$N resulting in phase-pure La$_{0.9}$Y$_{0.1}$Ta^{IV}O$_2$N, La$_{0.75}$Y$_{0.25}$Ta^{IV}O$_2$N, and La$_{0.7}$Y$_{0.3}$Ta^{IV}O$_2$N. By using microcrystalline YTaO$_4$ together with an unconventional ammonolysis protocol we synthesized the highest reported weight fraction (82(2) wt%) of perovskite-type YTa(O,N)$_3$. Ta^{4+} in La$_{1-x}$Y$_x$Ta^{IV}O$_2$N was verified by X-ray photoelectron spectroscopy (XPS) and X-ray near edge absorption structure (XANES) analysis. Density functional theory (DFT) calculations revealed a transparent conductor-like behavior explaining the unusual red/orange color of the Ta^{4+}-containing perovskites. In combination with crystal structure analysis the DFT calculations identified the orthorhombic strain as main descriptor for the unexpected trend of the optical bandgap ($E_{G,x=0.3} \approx E_{G,x=0} < E_{G,x=0.1} < E_{G,x=0.25}$). Surface photovoltage spectroscopy (SPS) of particulate La$_{1-x}$Y$_x$Ta^{IV}O$_2$N (x = 0, 0.1, 0.25, 0.3) films revealed negative photovoltages at photon energies exceeding 1.75 eV, confirming that these materials are *n*-type semiconductors with effective bandgaps of ∼1.75 eV irrespective of the Y content. The photovoltage values increased with the Y content, suggesting an improved carrier generation and separation in the materials. However, increasing the Y content also slowed down the timescales for photovoltage generation/decay indicating trap states in the material. Based on our results, we suggest a significantly weaker as classically assumed impact of reduced *B*-site metal cations such as Ta^{4+} on the photovoltage and charge carrier recombination rate.

Introduction

Among other materials, perovskite-type oxynitrides AB(O,N)$_3$ have attracted much attention particularly as photocatalysts for direct solar water splitting (SWS).[1–10] Their perovskite-type structure is of great scientific and technological interest because it combines

distinctive resistance with a large compositional flexibility allowing a controlled variation of the electronic properties. Owing to their SWS-suited optical bandgaps of $E_g \approx$ 2 eV, the most thoroughly investigated perovskite-type oxynitrides contain La^{III} on the *A*-site and Ti^{IV} [11] or Ta^V [12–19] on the *B*-site. In former reports, often reduced transition metal (TM) ions such as reduced Ta species in Ta^{V}ON[20,21] or in LaTa^{V}ON$_2$[22] were the origin of a fast charge carrier recombination and with it of a poor SWS performance. In such cases the TM ions were handled as defects introducing donor levels close to the conduction band. It was shown that an elimination of these defects enhanced the SWS activity[20,21] and slowed down the charge carrier recombination. However, a still remaining question is how a material and the respective electronic band structure (*e.g.* non-degenerate *vs.* degenerate semiconductor) behaves, if only reduced TM ions (*e.g.* Ta^{4+}) as *B*-site cations are present. In accordance with experimental reports,[12,23–25] LaTaON$_2$ was identified as a promising candidate for SWS also by computational analysis of the bandgap.[26–28] However, DFT-based electronic band structure calculations showed that the energetic position of the conduction band minimum (CBM) of LaTaON$_2$ does not ideally fit to the redox potential of the water reduction reaction.[27] Instead, the perovskite-type oxynitride YTaON$_2$, which to the best of our knowledge has not been synthesized in single-phase yet, seems to be well-suited.[27] Contrary to LaTaON$_2$, its CBM is predicted to be appropriate for the overall

water splitting reaction.[27] Y-containing perovskite-type materials are only rarely studied[29–31] due to the presumable instability as reflected by the low tolerance factor t as defined by Li et al.[32], e.g. $t = 0.912$ for YTaON$_2$ and $t = 0.898$ for YTaO$_2$N. Geometric considerations (extension of Goldschmidt's tolerance factor) locate YTaON$_2$ on the border of the existence field of perovskite-type oxynitrides, whereas YTaO$_2$N is located more or less outside of the existence field.[32] This higher instability, as expressed by the slightly positive heat of formation,[27] combined with the favorable band edge position is supposed to result in an enhanced reactivity as found for other catalytic systems.[33,34] Additionally, the low tolerance factors of YTaO$_2$N and YTaON$_2$[32] require a strong tilting of the octahedral network classically leading to a widening of the optical bandgap and a reduced dispersion of the conduction band.[27,35] This allows the adjustment of the CBM to the requirements of the water splitting reaction as theoretically demonstrated for YTaON$_2$.[27] The predicted metastability with respect to the binary oxides and nitrides[27] makes it very challenging to synthesize perovskite-type YTa(O,N)$_3$, since typically a defect-fluorite-type phase YTa(O,N,□)$_4$ sometimes accompanied by small amounts of perovskite-type phase was observed.[36–39]

We have recently reported on the controlled formation of the perovskite-type oxynitrides LaTa^{IV}O$_2$N and LaTa^{V}ON$_2$ by a precursor microstructure controlled ammonolysis.[14] A similar concept can also be applied to the synthesis of yttrium tantalum oxynitrides. In literature, the usage of a nanocrystalline oxide precursor (n-YTO) resulted in the formation of a defect-fluorite-type phase[30,36] with a suitable optical bandgap ($E_G \approx 2.2$ eV) but without photocatalytic activity for SWS.[30] The usage of microcrystalline YTaO$_4$ (m-YTaO$_4$) allowed the formation of a low crystallized perovskite-type main phase together with defect-fluorite-type phase and Ta$_3$N$_5$ impurities.[30] Attempts to enhance the crystallinity by raising the ammonolysis temperature resulted in the transformation to a defect-fluorite-type main phase.[30] For potential photocatalysts for water splitting and photoanode materials for water oxidation under visible light not only band gap sizes and band edge positions[40–42] are important, also the efficiency of charge carrier separation plays an essential role. As one of the advanced analytical tools, surface photovoltage spectroscopy (SPS) is typically applied to investigate the photo-induced charge carrier separation in a material.[43–45] This method provides information about majority charge carrier type (electron or hole), effective bandgaps, charge transfer timescales, and reversibility.[46,47]

In this work, a precursor microstructure controlled ammonolysis was combined with the gradual substitution of Y^{3+} for La^{3+} to tackle the synthetic challenge of forming YTa(O,N)$_3$. This produced the before unknown perovskite-type oxynitride family members La$_{1−x}$Y$_x$TaO$_2$N (x = 0.1, 0.25, 0.3) and, for $x = 1.0$, a mixture of perovskite-type main phase (w = 82(2) wt%) and defect-fluorite-type secondary phase (w = 18(2) wt%). The expected increasing distortion of the octahedral network induced by increasing Y content ($x \leq 0.3$) was confirmed by Rietveld refinements of high-resolution powder X-ray diffraction (HR-PXRD) patterns. However, diffuse reflectance spectroscopy (DRS) revealed a widening of the optical bandgap only up to $x = 0.25$

indicating that for La$_{1−x}$Y$_x$TaO$_2$N ($x \leq 0.3$) the distortion of the octahedral network is an insufficient descriptor for the bandgap size. Instead it seems that the level of orthorhombic strain ε is crucial for the resulting bandgap. In all synthesized La$_{1−x}$Y$_x$Ta^{IV}O$_2$N (x = 0.1, 0.25, 0.3) compounds the presence of Ta^{4+} as main oxidation state was confirmed via X-ray photoelectron spectroscopy (XPS) and X-ray near edge absorption structure (XANES) analysis, respectively. Superconducting quantum interference device (SQUID) measurements were used to characterize the magnetic properties. Density functional theory (DFT) calculations revealed a different band structure for La$_{1−x}$Y$_x$Ta^{IV}O$_2$N in comparison to LaTa^{V}ON$_2$ pointing to a transparent conductor-like behavior with a bandgap in the first case. The experimentally determined optical bandgaps of around 1.9 eV and low optically active defect concentrations of LaTa^{IV}O$_2$N[14] and La$_{1−x}$Y$_x$Ta^{IV}O$_2$N make these d^1 materials interesting as potential photocatalysts and as model system to study the influence of reduced B-site cations on the photo-induced charge carrier separation processes. SPS measurements revealed n-type semiconducting behavior of La$_{1−x}$Y$_x$TaO$_2$N upon visible light exposure and similar effective bandgaps regardless of the Y content. However, small Y contents had the fastest reversible charge carrier dynamics whereas higher contents decelerated it. One reason might be the level of tilting of the octahedral network and elongation of the octahedra. Importantly, surface photovoltages of up to −1 V were observed in La$_{1−x}$Y$_x$Ta^{IV}O$_2$N ($x \leq 0.3$), demonstrating the possibility of long-lived charge carriers in "Ta^{4+}-only" materials for the first time.

Results and Discussion

Ex situ ammonolysis of Y-substituted nanocrystalline lanthanum tantalum oxide (n-LTO) (10 mol% Y, 25 mol% Y, 30 mol% Y) with KCl flux addition lead to red La$_{0.9}$Y$_{0.1}$TaO$_2$N, orange La$_{0.75}$Y$_{0.25}$TaO$_2$N, and orange La$_{0.7}$Y$_{0.3}$TaO$_2$N after several cycles (Fig. 1). Characterization of the oxide precursors is described in the Supplementary Information (Fig. S1–S4 and Tab. S1–S4, Supplementary). The compositions of the oxynitrides were confirmed via inductively coupled plasma emission spectroscopy (ICP-OES) and hot gas extraction (HGE). Similar anionic ratios were previously reported for LaTaO$_2$N.[14] In addition, to prove the observed anionic ratio of O : N = 2 : 1 during *in situ* experiments in Y-substituted LaTaO$_2$N *in situ* ammonolysis with selected termination experiments and a subsequent reoxidation experiment by TGA was performed. The mass changes associated with *in situ* ammonolysis of 10 mol% Y-substituted n-LTO were similar to those previously reported for pure n-LTO[14] (Fig. S5, Supplementary). However, the specific surface area of 9 m²/g for 10 mol% Y-substituted n-LTO compared to 7 m²/g for n-LTO[14] was apparently high enough to achieve the desired O : N ratio of 2 : 1. This was confirmed via HGE measurements. Hence, the earlier assumption that ammonolysis of oxide precursors exhibiting a higher specific surface area leads to oxynitrides with a higher oxygen content[14] could also be demonstrated for 10 mol% Y-substituted LaTaO$_2$N. Additionally, the assumed "soft" topotactic reaction[14] via an intermediate in space group $Cmc2_1$ (alternative description $A2_1am$) which was suggested for LaTaO$_2$N could be observed for
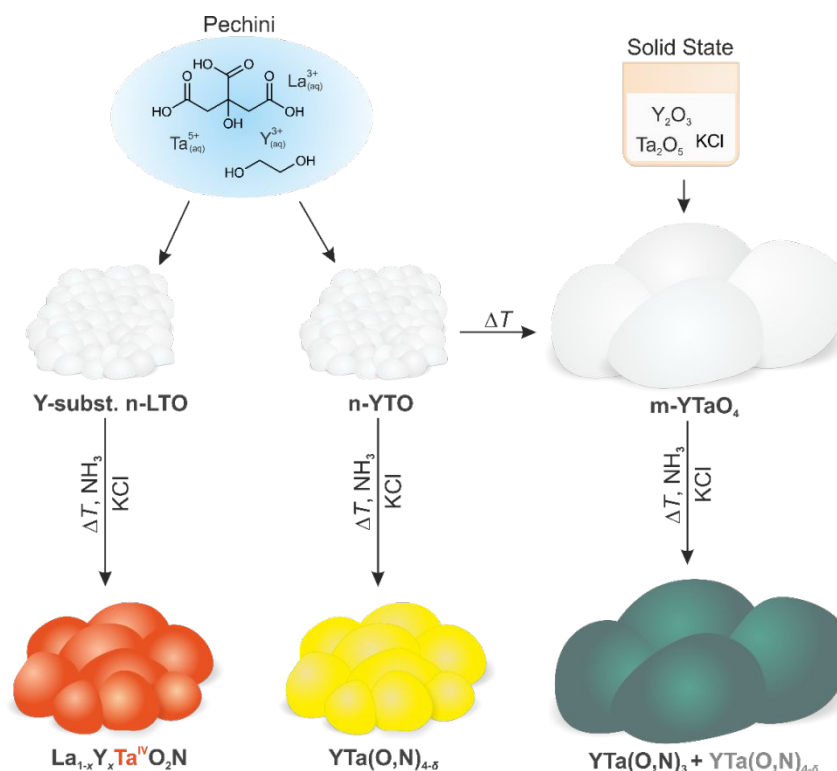
Fig. 1. Schematic synthesis paths from Y-substituted nanocrystalline lanthanum tantalum oxide (Y-subst. n-LTO), nanocrystalline yttrium tantalum oxide (n-YTO), and microcrystalline yttrium tantalate (m-YTaO$_4$) to the respective oxynitrides.

$La_{0.9}Y_{0.1}TaO_2N$. By chemical analysis and PXRD the black colored intermediate at 1187 K in space group $Cmc2_1$ was identified as $La_{0.9}Y_{0.1}TaO_{2.76(8)}N_{0.48(1)}\square_{0.75(9)}$ (Fig. S5, Fig. S6, and Tab. S5, Supplementary). After *in situ* ammonolysis at 1223 K for 10 h and at 1273 K for 14 h, respectively, subsequent reoxidation of $La_{0.9}Y_{0.1}TaO_2N$ to $La_{0.9}Y_{0.1}TaO_4$ was carried out under synthetic air. The observed mass change of +4.94 % was close to the calculated value of Δm_{calc} = +5.0 % (reoxidation of $La_{0.9}Y_{0.1}TaO_2N$ to $La_{0.9}Y_{0.1}TaO_4$) confirming an O : N ratio of 2 : 1 during *in situ* experiments. For higher Y-substituted n-LTO (25 mol% Y and 30 mol% Y), it was found that repeated ammonolysis cycles at 1273 K for 14 h with KCl flux addition (Fig. 1) were required to achieve single phase oxynitrides. *In situ* ammonolysis studies were abandoned in these cases for the protection of the TGA device.

HR-PXRD patterns of $La_{1-x}Y_xTaO_2N$ (x = 0.1, 0.25, 0.3) revealed that all three compounds were phase pure and adopted the space group *Imma* (Fig. S7 a)–c), Tab. S6, Supplementary). LaTaO$_2$N has already been reported to have the same space group.[14] In addition to HR-PXRD, $La_{0.9}Y_{0.1}TaO_2N$ was also studied by neutron diffraction (ND) in order to receive additional information about the space group and a potential anionic long-range order (Fig. S8, Tab. S7, Supplementary). The refined ND data could give no indications of an anionic long-range order. The absence of long-range ordering is in agreement with crystal structure data reported in literature.[48] Analysis of the unit cell parameters and unit cell volume obtained by Rietveld refinements of the HR-PXRD data showed that increasing Y substitution has two

clear effects: a continuous decrease of the unit cell volume (Tab. 1) and a higher level of tilting in the octahedral network (Tab. S8 a), Supplementary) due to the smaller ionic radius[32,49] of Y^{3+}.

The enhanced tilting of the [Ta(O,N)$_6$]$^{z-}$ octahedron due to partial Y^{3+} substitution is well-known for [B(O,N)$_6$]$^{z-}$ (B = Ti, Zr)[31] and can be visualized as a continuous reduction of the average Ta–(O/N)–Ta angles in $La_{1-x}Y_xTaO_2N$ (x = 0.1, 0.25, 0.3) (Tab. S8 a), Supplementary). Moreover, the Ta–(O/N) bond lengths in axial direction (*b*-axis) increase with increasing Y content leading to an elongation of the octahedron (Fig. S9 and Tab. S8 b), Supplementary). At the same time, the Ta–(O/N) bond lengths in equatorial direction (*c*-axis) decrease by increasing Y^{3+} content (Tab. S8 b), Supplementary). The

Tab. 1. Unit cell parameters, volumes, and orthorhombic strain ε of $La_{1-x}Y_xTaO_2N$ ($0 \leq x \leq 0.3$) in space group type *Imma*.

Unit Cell Parameter	LaTaO$_2$N[14]	La$_{0.9}$Y$_{0.1}$TaO$_2$N	La$_{0.75}$Y$_{0.25}$TaO$_2$N	La$_{0.7}$Y$_{0.3}$TaO$_2$N
a (Å)	5.7158(5)	5.7093(2)	5.6993(5)	5.7044(2)
b (Å)	8.0645(5)	8.0563(2)	8.0845(3)	8.0908(2)
c (Å)	5.7442(4)	5.7322(2)	5.6901(6)	5.6709(2)
V$_{cell}$ (Å³)	264.78(3)	263.66(1)	262.18(4)	261.73(2)
ε (-)	0.0025(1)	0.0020(1)	0.0008(1)	0.0029(1)

effects of elongation and distortion can be described by different amplitudes of the R_4^+ mode allowing a distortion of an initially cubic perovskite ($Pm\bar{3}m$) along [111] leading directly to the observed symmetry lowering to *Imma*. Even though there is already a significant tilting level reached, the HR-PXRD data suggest that the solubility limit of Y^{3+} is not yet surpassed up to $x = 0.3$ in $La_{1-x}Y_xTaO_2N$ (Fig. 2 a)).

For $LaTa^{IV}O_2N$ and $LaTa^VON_2$[14] the oxide precursor microstructure played an important role which phase is formed. The same applies for the reaction of the nanocrystalline yttrium tantalum oxide (n-YTO) to its oxynitride. In agreement with literature reports[30,36,37], it was not possible to prepare perovskite-type $YTa(O,N)_3$ by using n-YTO as precursor. Even by using an expanded tested parameter array for the ammonolysis temperature (from 973 K to 1373 K) in combination with n-YTO as precursor, only the formation of a defect-fluorite-type oxynitride phase was possible. In Figure S10 b), Supplementary, the yellowish, defect-fluorite-type $Y_{0.96(2)}Ta_{1.05(2)}O_{0.85(1)}N_{1.38(2)}\square_{1.82(3)}$ synthesized at 1023 K - containing highly reduced Ta - is shown as an example. Because, the here used n-YTO contains smaller crystallites caused by using a calcination temperature of 873 K instead of 1023 K (Si *et al.*[30]) - the onset of the applied ammonolysis reaction lowered at least by 50 K. In contrast, by using a microcrystalline yttrium tantalum oxide (m-YTaO$_4$) (Fig.

S10 c), Supplementary), it was possible to synthesize a well-crystalline perovskite-type main phase $YTa(O,N)_3$ in space group *Pnma* ($w = 82(2)$ wt%) next to $YTa(O,N,\square)_4$ ($w = 18(2)$ wt%) without XRD-detectable traces of binary nitrides such as Ta_3N_5 (Fig. S10 d), Supplementary). In this study, the usage of a microcrystalline precursor in combination with a higher ammonolysis temperature of 1373 K prior to a cycle at 1273 K and a larger ammonia gas flow as in ref. [30] allowed the perovskite-type phase formation. In agreement with the predictions based on the tolerance factor t[32] mentioned above $YTa(O,N)_3$ crystallized as orthorhombic perovskite phase but in contrast to $La_{1-x}Y_xTaO_2N$ in space group *Pnma*. This might be due to either the unknown O : N ratio or the smaller effective ionic radius of Y^{3+} compared to La^{3+}. Regarding the dual phase nature of this sample, a determination of the nitrogen content of the individual phases by chemical analysis is not applicable. By diffraction methods a definitive answer could not be provided, as the X-ray scattering contrast between O^{2-} and N^{3-} is too low and not enough material was available for ND measurements.

An increase of the specific surface area (S_{BET}) was observed for $La_{1-x}Y_xTaO_2N$ ($x = 0.1, 0.25, 0.3$) by comparing the synthesized oxide precursors (9 m²/g – 14 m²/g) with the respective oxynitrides (18 m²/g – 28 m²/g). SEM images (Fig. 2 b)) depicted morphologies
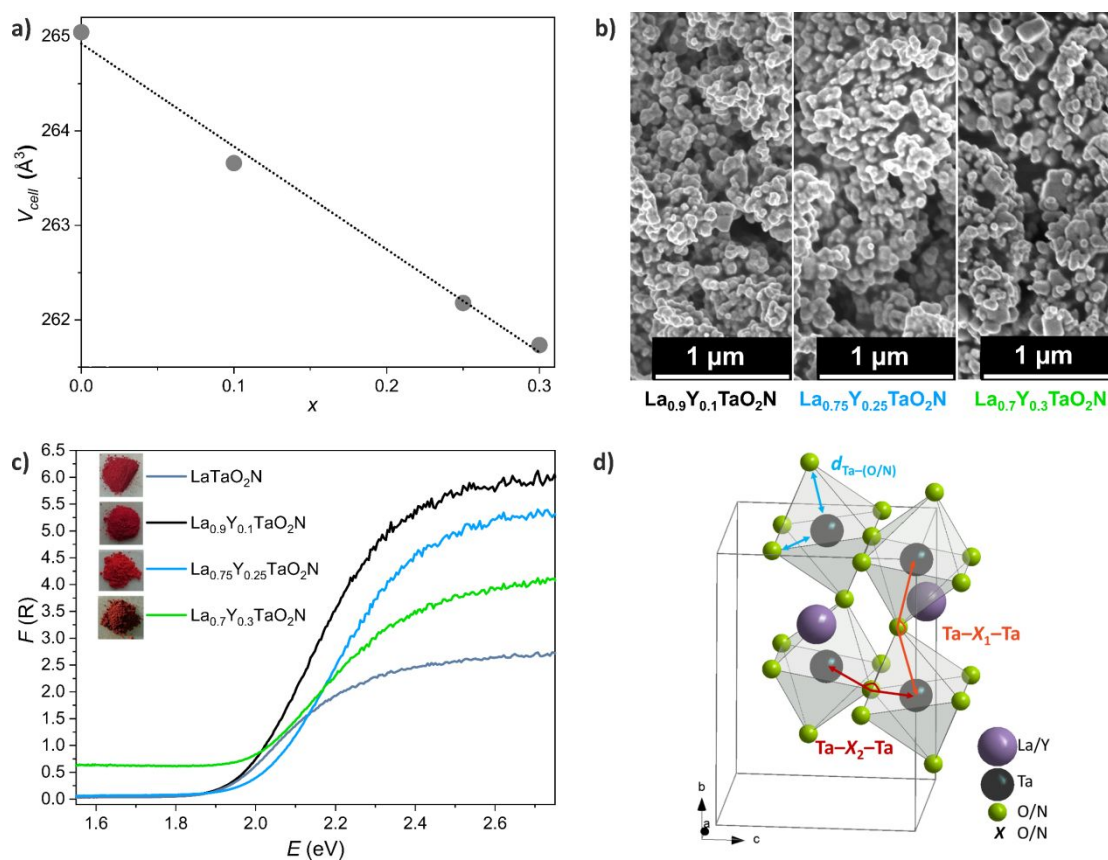
Fig. 2. a) Vegard's plot of the refined unit cell volume of $La_{1-x}Y_xTaO_2N$ ($x = 0.1, 0.25, 0.3$); for $x = 0$ the unit cell volume of $LaTaO_2N$[14] was used as reference. b) SEM images of $La_{1-x}Y_xTaO_2N$ ($x = 0.1, 0.25, 0.3$). c) DRS spectra of $La_{1-x}Y_xTaO_2N$ ($x = 0, 0.1, 0.25, 0.3$) plotted as Kubelka-Munk curves together with photographs of the received powders. d) $La_{1-x}Y_xTaO_2N$ unit cell edges and selected $[Ta^{IV}(O,N)_6]^{z-}$ octahedra with indicated Ta–$X_{1,2}$–Ta angles (with $X = O/N$) and $d_{Ta-(O/N)}$ distances. The O and N anions are displayed with a reduced radius for visibility reasons.

similar to that of LaTaO$_2$N[14] with visibly larger primary particle sizes compared to the respective oxides (Fig. S2 a)–c), Supplementary).

In addition to the decrease of the unit cell volume and the increase of the distortion of the octahedral network also the observed color change from red to orange (Fig. 2 c)) indicated a widening of the bandgap. DRS measurements and applying the Kubelka-Munk conversion[50] showed a slight change of the optical bandgap from 1.90 eV (LaTaO$_2$N) to 1.96 eV (La$_{0.75}$Y$_{0.25}$TaO$_2$N) with increasing Y substitution. In contrast La$_{0.7}$Y$_{0.3}$TaO$_2$N (E_G = 1.88 eV) did not follow this trend even though the average Ta–(O/N)–Ta angle was further decreased (Tab. S8 a), Supplementary). The samples La$_{0.9}$Y$_{0.1}$TaO$_2$N (E_G = 1.92 eV) and La$_{0.75}$Y$_{0.25}$TaO$_2$N (E_G = 1.96 eV) showed the same high color brilliance as LaTaO$_2$N.[14] In contrast, La$_{0.7}$Y$_{0.3}$TaO$_2$N has a brownish tone originating from optically active defects. The obtained behavior of the bandgap size upon partial Y^{3+} substitution is more complex than initially expected and cannot be simply explained by one effect. In La$_{1−x}$Y$_x$TaO$_2$N (x = 0, 0.1, 0.25, 0.3) multiple effects play a distinctive role: i) the effect of distortion of the octahedral network (decreasing average Ta–(O/N)–Ta angles, (Fig. 2 d), Tab. S8 a), Supplementary) typically related with a widening of the bandgap and ii) the elongation of the octahedra (increasing Ta–(O,N) bond lengths in axial direction, Tab. S8 b), Supplementary) leading to a smaller bandgap. These counteracting effects can be seen in the unexpected trend $E_{G,x=0.3} \approx E_{G,x=0} < E_{G,x=0.1} < E_{G,x=0.25}$ of the optical bandgap. The above mentioned R_4^+ mode is able to simultaneously describe both structural effects in La$_{1−x}$Y$_x$TaO$_2$N (x = 0, 0.1, 0.25, 0.3). Based on DFT calculations using the fixed, experimentally determined

orthorhombic strain only a slight variation of the R_4^+ mode amplitude by about 10 % upon partial Y^{3+}-substitution was observed. This is in accordance with the determined alteration of the unit cell parameters, bond angles and lengths of the materials (Tab. 1, S8, Supplementary), and the small resulting effect of the distortion of the octahedral network on the bandgap size. However, the experimentally observed changes in the bandgap data require a more complex description. The obtained variation of the unit cell parameters with the Y content x together with the different ionic radii of the A-site cations (r(La^{3+}) and r(Y^{3+})) resulted in an irregular variation of the orthorhombic strain ε - as defined in equation (1)[51] - of the oxynitrides La$_{1−x}$Y$_x$TaO$_2$N ($x \leq 0.3$) (Tab. 1).

$$\varepsilon = \left| \frac{(a-c)}{(a+c)} \right| \qquad (1)$$

For La$_{1−x}$Y$_x$TaO$_2$N ($x \leq 0.3$) the effect of the strain on the bandgap seems to dominate in comparison to the effects (distortion and elongation) resulting from a change in the amplitude of the R_4^+ mode. A clear correlation between ε and E_G can be obtained in the following way that a larger strain is leading to a smaller band gap and vice versa. Consequently, La$_{0.7}$Y$_{0.3}$TaO$_2$N has the smallest band gap within the series because it has the largest strain, while for La$_{0.75}$Y$_{0.25}$TaO$_2$N the smallest strain but the largest bandgap is observed. In comparison to perovskite-type oxides ABO$_3$ the effect of strain on the resulting bandgap in perovskite-type oxynitrides AB(O,N)$_3$ is much more complex and, experimentally far less investigated. DFT calculations suggest the strain is an important
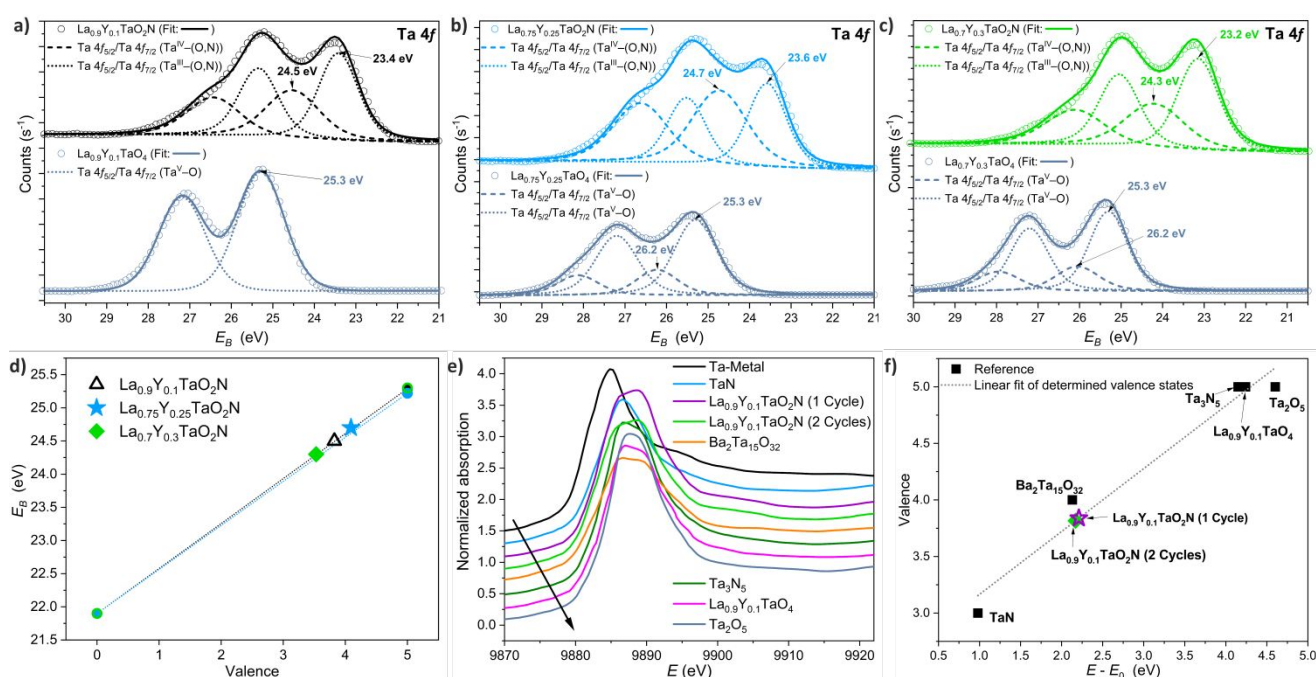
Fig. 3 a)-c) XPS spectra of the Ta $4f$ region of La$_{1−x}$Y$_x$TaO$_2$N (x = 0.1, 0.25, 0.3). Microcrystalline La$_{0.9}$Y$_{0.1}$TaO$_4$ was used as reference for Ta^{5+} and to determine the chemical shift after ammonolysis. d) The point charge model[55,56] was applied to the spectra as described in Bubeck *et al.*[14] e) Normalized X-ray absorption at the Ta L_{III}-edge as function of energy for all measured compounds and f) valence determination applying the inflection method: plot of the energy shift respective to Ta^0 against the valence for all measured compounds.

Tab. 2. Binding energies of the Ta $4f$ region of La$_{1-x}$Y$_x$TaO$_2$N (x = 0.1, 0.25, 0.3) with the respective binding characters determined *via* the point charge model.

Compound	$E_{B,\text{Ta }4f7/2}$ (eV)	$E_{B,\text{Ta }4f5/2}$ (eV)	Binding Character
La$_{0.9}$Y$_{0.1}$TaO$_2$N	23.4	25.4	Ta^{III}–(O,N)
	24.5	26.4	Ta^{IV}–(O,N)
La$_{0.75}$Y$_{0.25}$TaO$_2$N	23.6	25.5	Ta^{III}–(O,N)
	24.7	26.6	Ta^{IV}–(O,N)
La$_{0.7}$Y$_{0.3}$TaO$_2$N	23.2	25.1	Ta^{III}–(O,N)
	24.3	26.2	Ta^{IV}–(O,N)

parameter for the band structure, since a variation of the strain state can cause a change of the bandgap of more than 1 eV[52] (for SrTiO$_3$[53] in comparison just 0.1 eV). For ABO$_3$ the application of both compressive and tensile stress results in a reduction of the bandgap.[52] For the oxynitrides such as LaTiO$_2$N, CaTaO$_2$N, SrTaO$_2$N, and BaTaO$_2$N a multiparameter dependency of the bandgap from the strain is observed by DFT calculations. The application of both strains (compressive or tensile) to these materials can either cause a blue-shift or a red-shift of the bandgap depending on the following parameters: i) unit cell volume (controlled mainly by the A-site cation), ii) energetic position and crystal field splitting of the B-site cations (3d vs. 5d) with respect to the O/N 2p orbitals, iii) direction of applied strain in relation to the crystal axis, iv) type and degree of (local) O/N ordering (cis *vs*. trans), and v) the level of octahedral rotation and the inversely correlated ferroelectric displacements.[52,54] Therefore, more combined theoretical and experimental investigations are required in the future to establish a more generally valid model to describe the interrelation between strain and bandgap in perovskite-type oxynitrides. Besides the bandgap size also the band edge positions must match with the redox potentials of H$_2$O for potential SWS catalysts. The conducted electrochemical experiments and calculations (Tab. S9, Supplementary) did not deliver a conclusive answer so far if the band edge positions of La$_{1-x}$Y$_x$Ta^{IV}O$_2$N are suitable for SWS. The detailed analysis results can be found in Table S9, Supplementary. Therefore, in the following we focus on the charge carrier separation behavior and the effects of Ta^{4+} on it.

Like for the samples La$_{1-x}$Y$_x$TaO$_2$N (Fig. 2 c)) also the defect-fluorite-type oxynitride YTa(O,N,□)$_4$ (Tab. S10, Supplementary) showed a different coloration than expected from the presence of Ta ions below the 5+ state. Nonetheless, the determined optical band gap of E_G = 2.2 eV (Fig. S11, Supplementary) was still in agreement with literature reports.[26,30] At lower energies than the optical bandgap no increasing background was observed pointing to a low optically active defect concentration as observed for the La-containing perovskites. In contrast, the color of the mixture of the perovskite-type YTa(O,N)$_3$ phase (greenish black) indicated a high concentration of optically active defects besides an optical bandgap of around 2 eV.

The composition of La$_{1-x}$Y$_x$TaO$_2$N (x = 0.1, 0.25, 0.3) provides two possibilities for the oxidation state of Ta (Fig. 3 a)–c)). Either it has an overall oxidation state of 4+ or it is present as 3+ and 5+ in equal shares. For a detailed evaluation of the oxidation state of Ta we analyzed the Ta $4f$ regions of the XPS spectra. The binding energies of the Ta $4f_{7/2}$ and Ta $4f_{5/2}$ orbitals (Tab. 2) obtained from the spectra (survey spectra in Fig. S12, Supplementary) were consistent with the values determined for the Ta^{4+} compound LaTa^{IV}O$_2$N[14]. As recently reported for LaTaO$_2$N[14] by applying the point charge model[14,55,56], a chemical shift to lower binding energies by more than 0.3 eV indicates a change of the Ta oxidation state from 5+ to 4+. Therefore, the binding energies of La$_{1-x}$Y$_x$TaO$_2$N (x = 0.1, 0.25, 0.3) are consistent with either a Ta^{IV}–(O,N) or a Ta^{III}–(O,N) binding character (Tab. 2). The Ta $4f_{7/2}$ binding energies for the Ta(V)–O binding character of microcrystalline La$_{0.9}$Y$_{0.1}$TaO$_4$ ($E_{B,\text{Ta}4f7/2}$ = 25.3 eV), La$_{0.75}$Y$_{0.25}$TaO$_4$ ($E_{B,\text{Ta}4f7/2}$ = 25.2 eV) and La$_{0.7}$Y$_{0.3}$TaO$_4$ ($E_{B,\text{Ta}4f7/2}$ = 25.3 eV) were used as Ta^{5+} references, respectively (Fig. 3 a)–c)). In contrast to recent literature reports on LaTaON$_2$[12,14] and PrTaO$_2$N[12] our data did not provide any evidence of the presence of Ta^{5+} in La$_{1-x}$Y$_x$TaO$_2$N (x = 0.1, 0.25, 0.3). The $E_{B,\text{Ta(V)}4f7/2}$ values reported there (e.g. 28.03 eV[12], 27.46 eV[12], and 25.0 eV[14]) significantly exceed our measurement results. A massive peak broadening or significant double peak splitting described for the above mentioned compounds[12] was not observed either in our measurement data. Thus, the observed anionic composition of La$_{1-x}$Y$_x$TaO$_2$N can be explained by the presence of Ta^{4+} (d^1 state). The slightly lower binding energy of the Ta^{IV}–(O,N) binding character in La$_{0.7}$Y$_{0.3}$TaO$_2$N can be attributed to the higher number of ammonolysis cycles required at 1273 K leading to an enhanced reduction to Ta^{3+} at the surface and nitrogen enrichment[14] in the chemical environment of the [Ta^{IV}(O,N)$_6$]$^{z-}$ octahedron.

Additionally, the N and O weight fractions were calculated from the peak areas of the respective fitted orbitals. O/N ratios of 2, 1.92, and 1.79 were determined for 10, 25 and 30 mol% Y-substitution in La$_{1-x}$Y$_x$TaO$_2$N, respectively. This matches quite well with the anionic compositions determined *via* reoxidation and HGE measurements (Tab. S11, Supplementary). The determined O/N ratios support the above given interpretation of the shifted binding energy by nitrogen enrichment in the surrounding of Ta. The small difference to the theoretical O/N ratio of 2 can also be resulting from the overlapping of N 1s, Y 3s, and Ta 4p orbitals.

Given by the small mean free path of photo-emitted electrons (normally between 1 and 10 nm[57]) XPS is a surface-sensitive method. Therefore, the assumed change of the oxidation state from Ta^{5+} to Ta^{4+} during ammonolysis of the oxide precursors was additionally studied in the bulk *via* XANES at the Ta-L_{III} edge (Fig. 3). As reference materials, well-defined Ta oxidation states of Ta metal, TaN, Ba$_2$Ta$_{15}$O$_{32}$, Ta$_3$N$_5$, La$_{0.9}$Y$_{0.1}$TaO$_4$, and Ta$_2$O$_5$ were used for the XANES data analysis. The samples La$_{0.9}$Y$_{0.1}$TaO$_2$N (ammonolyzed once at 1223 K) and La$_{0.9}$Y$_{0.1}$TaO$_2$N (ammonolyzed twice: 1x at 1223 K, 1x at 1273 K + KCl flux addition) were measured and their determined normalized absorption was plotted against the energy (Fig. 3 e)). The Ta-L_{III} absorption edges of both La$_{0.9}$Y$_{0.1}$TaO$_2$N samples are located in-between the Ta-L_{III} absorption edges of the Ta^{3+} and Ta^{5+} reference

materials and close to the Ta-L_{III} absorption edge of $Ba_2Ta^{IV}_{15}O_{32}$, which had been synthesized according to Siegrist *et al.*[58] As expected, the absorption edge shifted to higher energies with increasing oxidation state of Ta.[59] According to Henderson *et al.*[57] a shift of the *L*-edges by about 1.5 eV/valence is expected. For Si even a shift of 2.2 eV/valence[57] was observed. In our case, a shift of 2.1–2.2 eV with respect to the Ta^0 reference was determined for $La_{0.9}Y_{0.1}TaO_2N$ (1 and 2 cycles). Since the oxidation state or valence state, respectively, is linearly correlated with the energy shift[57], an oxidation state between +3.8 and +3.9, close to the expected +4, was obtained in the bulk (Fig. 3 f)). Hence, a uniform oxidation state could be demonstrated for the bulk and the surface region. This finding is in good accordance with the anionic ratio of O : N = 2 : 1 obtained from chemical analysis and XPS data. On closer examination of the curve shapes of $La_{0.9}Y_{0.1}TaO_2N$, $Ba_2Ta_{15}O_{32}$, and $La_{0.9}Y_{0.1}TaO_4$, a double structure in the white line is visible. According to Rietveld refinements, Ta is surrounded by six anions in a distorted octahedral coordination suggesting a crystal field splitting. This crystal field splitting becomes obvious in the Ta-L_{III} transition since it probes the (partially) empty $5d$ states with electrons from the occupied $2p$ states.[60] Crystal field splitting values of 4 eV[60] and even $5.5 - 6$ eV[61] were reported for Ta^{5+} in $KTaO_3$ and Ta-substituted TiO_2 solid solutions, respectively. For both $La_{0.9}Y_{0.1}TaO_2N$ samples a smaller peak splitting of 2.5 eV was observed. This points to a lower oxidation state since oxidation state and crystal field splitting energy are correlated.[61] Additionally, distortion in the octahedral environment of the centered cation increases the crystal field splitting according to theoretical models.[57] Since the effective ionic radius of Ta^{4+} ($r_{eff}(Ta^{4+})$ = 0.68 Å[27]) is larger than that of Ta^{5+} ($r_{eff}(Ta^{5+})$ = 0.64 Å[27]) and the effective radius of K^+ ($r_{eff}(K^+)$ = 1.64 Å[27]) is larger than those of La^{3+} and Y^{3+}, the distortion in both $La_{0.9}Y_{0.1}TaO_2N$ samples is expected to be lower than that in $KTaO_3$. This is consistent with our measurements and the fact that $r_{eff}(Ta^{4+}) > r_{eff}(Ta^{5+})$ also explains the different peak splitting values of $La_{0.9}Y_{0.1}TaO_2N$ (2.5 eV) and $La_{0.9}Y_{0.1}TaO_4$ (2.8 eV).

The $5d^1$ electronic configuration of tantalum (Ta^{4+}) was further analyzed *via* SQUID measurements (Fig. S13 a) and b), Supplementary). The measured $M(H)$ curves reveal different saturation magnetizations of $3.46 \cdot 10^{-4}$ emu ($x = 0.1$) and of $9.19 \cdot 10^{-4}$ emu ($x = 0.25$) and are equivalent to effective magnetic moments of 0.0011 μ_B/Ta ($x = 0.1$) and 0.0031 μ_B/Ta ($x = 0.25$), respectively. Additionally, to the paramagnetism, $La_{0.75}Y_{0.25}Ta^{IV}O_2N$ showed a very small ferromagnetic-like contribution. To separate the observed ferromagnetic (FM) contribution, it was subtracted from the low temperature hysteresis of the sample. Similar FM-like contributions were also observed in other bulk non-magnetic materials, with nominal d^0 contribution, which were identified as non-stoichiometric surface states.[62–64] By applying a Brillouin-Function[65] fit (shown in the insets of Fig. S13 a), b) and c), Supplementary) to investigate the paramagnetism a magnetic moment of 2.1 μ_B for both samples was estimated. This is in contrast to the calculated small μ_B/Ta values for both samples, showing that just a tiny fraction of the Ta ions show paramagnetism with a moment of 2.1 μ_B. The determined 2.1 μ_B for both samples are consistent to surface related Ta^{3+} impurity ions ($5d^2$

with assumed 2 μ_B/magnetic ion), which were detected by XPS (Fig. 3 a)–c)). If we assume a 50 % presence of Ta^{3+} in the first 0.1 nm of each nanoparticle, we can calculate a surface to volume ratio with which the same reduced total μ_B/Ta is obtained. This results in typical particle sizes in the range of $100 - 300$ nm, consistent to the obtained SEM results in Figure 2 b). By calculating the quantitative amount of Ta^{3+} and Ta^{4+} for $x = 0.1$ one Ta^{3+} per 1914 Ta^{4+} ions and for $x = 0.25$ one Ta^{3+} per 670 Ta^{4+} ions are obtained, respectively. This confirms the small amount of Ta^{3+} and points to the suggested "Ta^{4+}-all" materials and that Ta^{3+} is just located on the samples' surface. A similar nearly non-magnetic behavior was already observed for $LaTa^{IV}O_2N$ and $LaTa^{V}ON_2$[14] and, hence, a similar orbital hybridization for $La_{1-x}Y_xTaO_2N$ is assumed. Fixed magnetic calculations at 0 K (Fig. S13 d), Supplementary) showed for $LaTa^{V}ON_2$, $LaTa^{IV}O_2N$, and $La_{0.75}Y_{0.25}Ta^{IV}O_2N$ a positive energy upon addition of a magnetic moment pointing to a non-magnetic behavior of the respective oxynitrides.

The simultaneous presence of reduced *B*-site cations with d^1 electron configuration and a significant optical band gap is quite unusual and might point to a transparent conductor-like behavior. Indeed, from the electronic band structure and consequently in the density of states (DOS) the existence of metallic Ta $5d$ states was visible (Fig. S14, Supplementary). Such behavior is well-known from heavily-doped degenerated semiconductors such as the transparent conducting fluorine-doped tin oxide (FTO)[66] and indium-doped tin oxide (ITO)[67]. Another even closer related example is the red metallic photocatalyst $Sr_{1-x}NbO_3$ (Nb^{4+}) with an optical band gap of 1.9 eV showing a very similar electronic band structure[68] as $La_{1-x}Y_xTaO_2N$. A detailed discussion of the electronic band structure can be found in the Supplementary Information, section "Electronic band structure". The calculated optical conductivity[61] of $La_{1-x}Y_xTaO_2N$ (Fig. 4a)) agreed as well with this by showing a strong increase of the conductivity at energies below around 0.5 eV pointing to the presence of metallic states. However, at energies higher than 3.5 eV a second increase of the calculated optical conductivity was obtained caused by the absorption of photons with an energy higher than the bandgap. For $LaTa^{V}ON_2$ as expected no absorption was obtained at energies lower than the bandgap in the calculated optical conductivity due to the $5d^0$ electronic configuration of Ta^{5+} (Fig. 4 a)).

The ability of the oxynitrides to separate photogenerated charge carriers under illumination was studied by surface photovoltage spectroscopy (SPS) of 800–1500 nm thick particulate films on fluorine doped tin oxide (FTO) substrates. The SPS data are presented in Fig. 4 b) and c) (for numerical data and photos of the films see Tab. S12 and Fig. S15, Supplementary). All $La_{1-x}Y_xTaO_2N$ films produced negative photovoltage ranging from −0.44 V to −1.01 V due to electron injection into the FTO substrate (Fig. 4 d). This indicates that all samples are *n*-type semiconductors. As can be seen from the exemplary calculated electronic band structure of $LaTa^{V}ON_2$ (Fig. S14 a), Supplementary) a direct bandgap was obtained. This is beneficial for light-driven applications and light absorption. In contrast, the band structures of $LaTa^{IV}O_2N$ and $La_{0.875}Y_{0.125}Ta^{IV}O_2N$ (Fig. S14 b) and c), Supplementary) point to a degenerate semiconductor. The maximum photovoltage was reached at 2.75 eV for most materials,
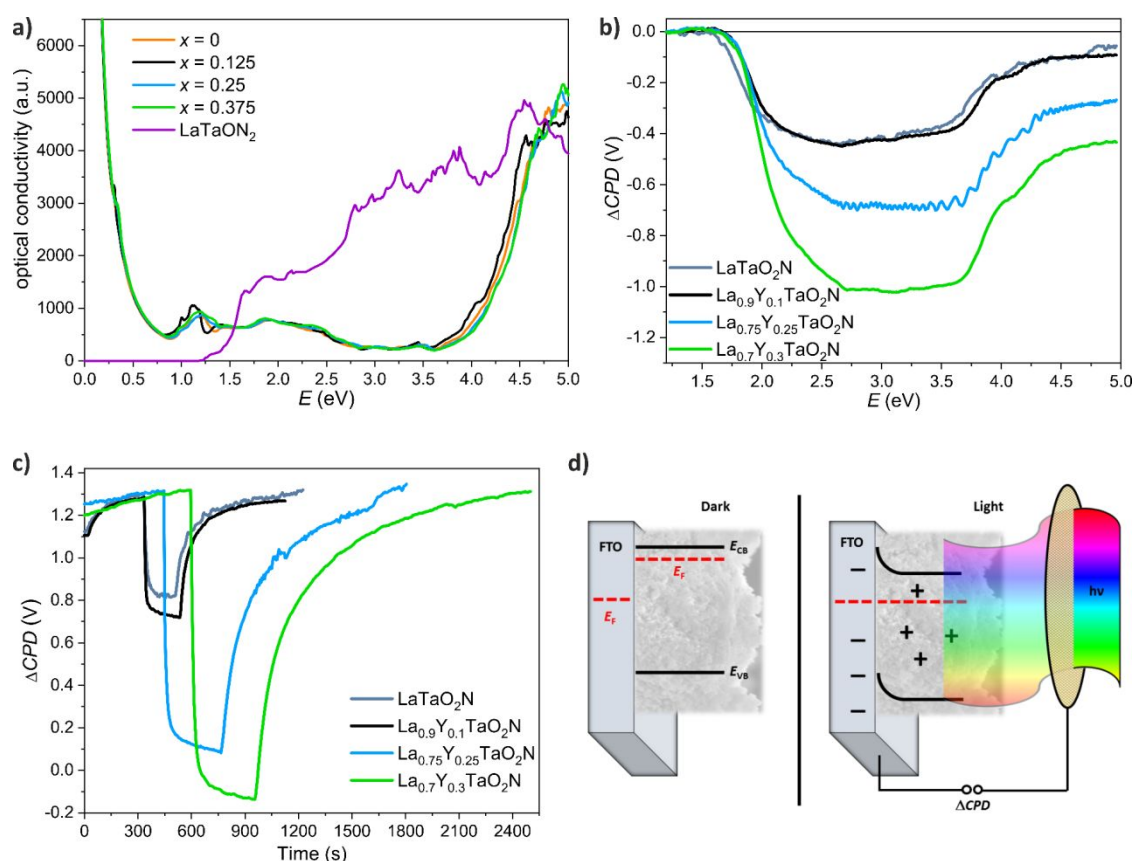
Fig. 4 a) Calculated optical conductivity of $La_{1-x}Y_xTaO_2N$ (x = 0, 0.125, 0.25, 0.375) and $LaTaON_2$ b) Surface photovoltage spectra (SPS) of all $La_{1-x}Y_xTaO_2N$ sample films on FTO. ΔCPD designates the contact potential difference change under illumination, i.e. the photovoltage. c) Chopped light scans of all $La_{1-x}Y_xTaO_2N$ samples under monochromatic illumination at 2.48 eV (on: ~300 – 600 s; off: ~500 – 960 s). d) Energy diagram of the $La_{1-x}Y_xTaO_2N$ /FTO interface before and after illumination.

which coincides with the maximum spectral emission intensity from the Xe-lamp (Fig. S16, Supplementary). The photovoltage value increases in the order $LaTaO_2N$, $La_{0.9}Y_{0.1}TaO_2N < La_{0.75}Y_{0.25}TaO_2N < La_{0.7}Y_{0.3}TaO_2N$, suggesting improved charge carrier separation for the more heavily Y-substituted samples. Based on tangential approximation of the major photovoltage feature, the effective bandgaps ranged from 1.65 eV to 1.78 eV. These values are 0.25 eV to 0.12 eV below the measured optical bandgaps of $E_G \approx 1.9$ eV for $La_{1-x}Y_xTaO_2N$ (x = 0, 0.1, 0.25, 0.3). The difference indicates a small concentration of visible light-active states near the band edges in the materials. These states are observable in SPS even though their concentration is too small to contribute to the visible absorption spectra. After concluding the SPS scan, the films were left in the dark until a stable voltage signal was achieved. Then, chopped light scans were applied under monochromatic illumination at 2.48 eV to examine the reversibility of photo-induced charge separation in each material (Fig. 4 c)). The time constants, τ, in Table S12 (Supplementary) correspond to the amount of time required to achieve 63.21% of the final photovoltage after turning the light on or off. The sample $La_{0.9}Y_{0.1}TaO_2N$ (x = 0.1) had the fastest photovoltage generation/decay (τ_{on} = 7.62 s, τ_{off} = 73 s) compared to *e.g.* the Y-free

sample (τ_{on} = 22 s, τ_{off} = 89 s), suggesting that the introduction of a small amount of Y improves the charge carrier transport rate. The τ_{on} and τ_{off} values of the other samples increased with increasing Y content, meaning charge carrier transport became slower. Besides changes in the electronic structure of the material, induced by Y-substitution, other reasons for the increased τ_{on} times could be an increase in the particle packing density in the films, resulting from a change in particle morphology upon substitution with Y^{3+}, or a change in the concentration of the hole traps at the particle surfaces, allowing faster trapping of photoholes in the Y-substitution materials. A strong surface state-dependent photovoltage formation due to hole trapping has been observed before *e.g.* for Fe_2O_3 nanorod arrays.[69] The larger photovoltage values correspond to an enhanced separation of the photogenerated charge carriers. It has already been reported that the presence of reduced *B*-site metal cations such as Ti^{III} [70,71] or Ta^{IV} [72] can cause fast recombination of photogenerated electrons and holes vanishing the photovoltage. However, based on the SPS data in Fig. 4 b), the Ta^{4+}-only materials $La_{1-x}Y_xTa^{IV}O_2N$ (x = 0, 0.1, 0.25, 0.3) are able to generate and separate charge carriers based on the photovoltage. A reason for this might be hidden in beneficial effects caused by the octahedral network

distortion and elongation of the $[Ta^{IV}(O,N)_6]^{2-}$ octahedra as well as the altered electronic band structure overcompensating the traditionally assumed detrimental effect of Ta^{4+}.

Conclusion

In conclusion, the perovskite-type d^1 materials $La_{0.9}Y_{0.1}Ta^{IV}O_2N$, $La_{0.75}Y_{0.25}Ta^{IV}O_2N$, $La_{0.7}Y_{0.3}Ta^{IV}O_2N$ were produced *via ex situ* ammonolysis of 10 mol%, 25 mol%, and 30 mol% Y-substituted n-LTO – achieved *via* Pechini method – successfully expanding the applicability of our recently published precursor microstructure controlled ammonolysis. Using n-YTO and m-YTaO$_4$ as precursors allowed to synthesize either a defect-fluorite-type phase or the highest weight fraction of perovskite-type YTa(O,N)$_3$ known so far next to some remaining YTa(O,N,□)$_4$. In the latter, an unconventional initial ammonolysis step at high temperature was required. For visible light-driven energy conversion processes the bandgap size is a crucial material parameter. In this context, the mixture of YTa(O,N)$_3$ and defect-fluorite phase showed a greenish black color with an optical band gap of around 2 eV and a broad range absorption. In contrast, the pure defect fluorite-phase showed a yellowish color with a well-defined optical bandgap of 2.2 eV. In $La_{1-x}Y_xTa^{IV}O_2N$ ($x \leq 0.3$) increasing Y substitution revealed an unexpected trend of the optical bandgap ($E_{G,x=0.3} \approx E_{G,x=0} < E_{G,x=0.1} < E_{G,x=0.25}$) with unusual colors ranging from red to orange. XPS and XANES data revealed that the oxidation state of Ta in $La_{1-x}Y_xTaO_2N$ is predominantly 4+. In accordance, DFT calculations showed the presence of metallic Ta $5d$ states next to a fundamental bandgap obvious from the calculated optical conductivity. The combination of crystal structure analysis and DFT calculations suggest orthorhombic strain as the main reason for the experimentally observed optical bandgap trends. The octahedral network distortion and elongation of the octahedra play additional roles.

Furthermore, SPS revealed an unexpected, remarkable photovoltage and a visible light-driven charge carrier separation even in the presence of reduced *B*-site cations, namely Ta^{4+} and Ta^{3+}. The increasing partial substitution of Y^{3+} for La^{3+} in $La_{1-x}Y_xTa^{IV}O_2N$ ($x = 0$, 0.1, 0.25, 0.3) indicated an improved charge carrier generation and separation for the "Ta^{4+}-all" materials on the basis of larger photovoltage values. These results confirm the possibility of photophysical charge separation in degenerate semiconductors with large free carrier concentrations (from Ta^{4+} states).

Experimental

Synthesis of Y-substituted n-LTO and $La_{1-x}Y_xTaO_2N$

Nanocrystalline Y-substituted n-LTO (x_Y = 10 mol%, 25 mol%, and 30 mol%) and n-YTO precursors were prepared by the same sol-gel-related method as described previously.[14] Y substitution was accomplished by providing an appropriate amount of $Y(NO_3)_3 \cdot 6H_2O$ (Alfa Aesar, 99.9 %) according to the mol% fraction ($x = 0$, 0.1, 0.25, 0.3, 1.0) in addition to $La(NO_3)_3 \cdot 6H_2O$ (Sigma Aldrich, 99.99 %) in a second Schlenk flask. Further details about the oxide precursors are summarized in the Supplementary Information. The oxynitrides La_{1-}

$_xY_xTaO_2N$ ($x \leq 0.3$) were prepared from the respective nanocrystalline oxide precursors *via* thermal gas flow (*ex situ*) ammonolysis as previously reported in detail[14]: 200 mg of the oxides were transferred into an Al_2O_3 boat and ammonolyzed once at 1223 K for 10 h under flowing NH$_3$ (300 mL/min, Westfalen AG, > 99.98 %). This was followed by repeated *ex situ* ammonolysis cycles with KCl flux addition (weight ratio 1:1) at 1273 K for 14 h until phase purity was achieved. The higher the Y substitution the more ammonolysis steps (up to 10) were required. For the synthesis of yttrium tantalum oxynitrides the precursors n-YTO and m-YTaO$_4$ were used. The m-YTaO$_4$ was prepared by a solid state reaction similar as in Bubeck *et al*.[14] For n-YTO the ammonolysis temperature was varied from 973 K to 1373 K keeping the reaction time constant at 14 h. m-YTaO$_4$ was ammonolyzed first at 1373 K for 10 h, second for 14 h at 1273 K with KCl flux addition using several repetitions. The ammonia flow rate was in both cases the same as for $La_{1-x}Y_xTaO_2N$ (300 mL·min^{-1}).

Caution: ammonia is a toxic and corrosive gas and have to be handled only by supervised and trained persons in special apparatus not allowing for emission of ammonia into the laboratory atmosphere.

Films of $La_{1-x}Y_xTaO_2N$ for Surface Photovoltage Spectroscopy

Fluorine-doped tin oxide (FTO) substrates (12-14 Ω/sq, MTI Corporation) were cleaned by sonication in acetone, methanol, isopropanol, and water (purified to about 18 MΩ·cm resistivity with a Nano-pure filtration system) for 10 min each, and dried in air. Separate suspensions of the $La_{1-x}Y_xTaO_2N$ powders in water with a concentration of 0.5 mg·mL^{-1} were prepared. After sonication for 15 minutes, 0.05 mL of each suspension was drop-coated onto the FTO substrates. The coverage area (0.5 cm × 0.5 cm) was controlled with a polyester masking tape (Cole Parmer). After drying at ambient temperature, the films were heated on a hot plate at 373 K for 90 min in air. Photos of the films are included in the Supporting Information. Films were between 800 nm and 1500 nm thick as determined with a stylus-type Veeco Dektak profilometer.

Density Functional Theory (DFT) Calculations

The DFT calculations were performed using the full potential local-orbital minimum-basis method as implemented in the FPLO code.[73,74] The exchange-correlation functional was parameterized using the generalized gradient approximation (GGA).[75] The lattice parameters and atomic positions were adopted from the experimental data in order to have a direct comparison. A 16×16×16k-mesh was used to guarantee a good convergence. Due to the limited size of the supercell a simplified model to implement the partial Y substitution was used by replacing 1, 2 or 3 La by Y. This resulted in $La_{0.875}Y_{0.125}TaO_2N$, $La_{0.75}Y_{0.25}TaO_2N$, and $La_{0.625}Y_{0.375}TaO_2N$ as representatives of $La_{0.9}Y_{0.1}TaO_2N$, $La_{0.75}Y_{0.25}TaO_2N$, and $La_{0.7}Y_{0.3}TaO_2N$, respectively. The virtual crystal approximation was applied to model the experimentally observed disordered mixture of O and N atoms in the oxynitrides. In order to understand the experimental SQUID measurements, fixed moment calculations are done with the resulting total energies with respect to the total magnetic moments of the unit cells shown in Fig. S9, Supplementary. The band structures for the supercells are unfolded into the Brillouin

zone of the primitive cell (Fig. S14, Supplementary), which allows to make a direct comparison. The optical conductivities are evaluated based on the complex dielectric functions including both the intraband and interband contributions.

Characterization

Powder X-Ray Diffraction (PXRD) measurements were carried out on a Rigaku Smartlab powder X-ray diffractometer using Ni-filtered Cu-$K\alpha_{1,2}$ radiation in order to examine the phase purity and crystal structure of the oxides and oxynitrides. High-resolution (HR) synchrotron radiation PXRD measurements of selected oxide and oxynitride samples were performed at the beam line ID22 of the European Synchrotron Radiation Facility (ESRF) in Grenoble, France. The diffraction data were analyzed by Rietveld refinements[76,77] using *FullProf.* 2k[78].

A potential long-range order of O and N in the $La_{0.9}Y_{0.1}TaO_2N$ sample was investigated *via* high resolution neutron diffraction at ambient temperature on SPODI at the Research Neutron Source Heinz Maier-Leibnitz (FRM II) in Garching, Germany.[79] Approximately 200 mg of the sample were loaded in a standard vanadium cylinder with 6 mm outer diameter. The measurement was carried out at a wavelength of λ = 1.54818(2) Å using a take-off angle of 155° of the (551) atomic plane of the Ge monochromator.

The cationic composition of the samples was studied by inductively coupled plasma emission spectroscopy (ICP-OES) on a Spectro Ciros CCD ICP-OES instrument. The anionic composition was determined by hot gas extraction (HGE) using an Eltra ONH-2000 analyzer. Each sample was measured at least three times.

In situ ammonolysis under flowing NH_3 (80 mL·min^{-1} NH_3 + 8 mL·min^{-1} Ar) was carried out *via* thermogravimetric analysis (TGA) on a Netzsch STA 449F3 Jupiter with a Perseus-coupled Bruker FTIR spectrometer (Alpha). The subsequent reoxidation of $La_{0.9}Y_{0.1}TaO_2N$ was done under synthetic air (50 mL·min^{-1} syn. air + 20 mL·min^{-1} Ar). To determine the oxidation state of Ta in $La_{1-x}Y_xTaO_2N$ and Y-substituted n-LTO X-ray photoelectron spectroscopy (XPS) was performed with a Thermo VG Theta Probe 300 XPS system (Thermo Fisher Scientific). The incident beam had a spot size of 400 μm and was monochromatic with micro-focused Al K_α radiation. A carbon tape was used as sample holder and a flood gun avoided undesirable charging effects. A Shirley-type inelastic background was chosen for background subtraction. The XPS spectra were analyzed as described previously.[14]

The morphology of the produced oxides and oxynitrides was investigated *via* scanning electron microscopy (SEM) (ZEISS GeminiSEM 500, 5 kV) using the in-lens detector.

UV-visible diffuse reflectance spectroscopy (DRS) was performed with a Carry 5000 UV–VIS NIR spectrophotometer. The baseline was measured with $BaSO_4$ as reference. The optical bandgap was estimated by using the Kubelka-Munk conversion[50] and applying the tangential method[14,32].

Nitrogen sorption was applied to obtain the data to determine specific surface areas of the materials. First, the samples were annealed at 393 K to remove adsorbed water. Adsorption and desorption isotherms were recorded at liquid nitrogen temperature with an Autosorb-1-MP (detection limit: S_{BET} > 1 m²/g) from Quantachrome Instruments. The specific surface areas were determined by the Brunauer-Emmet-Teller[80] (BET) method.

X-ray absorption near-edge structure (XANES) characterization was carried out at the Spanish beamline BM25A SpLine[81] at ESRF. Measurements were performed in transmission mode using three high precision ionization chambers and an ethanol-cooled (203 K) double Si(111) crystal monochromator with an energy resolution of $\Delta E/E$ = 1.4×10^{-4}. Samples were pelletized with cellulose for transmission measurements. The concentration of the samples was calculated to obtain an absorption jump of $\Delta\mu_{tot} \approx 1$ at the Ta L_{III}-edge (9.881 keV). XANES data were normalized using the Athena software package.[82]

Magnetometer surveys were carried out with a commercial VSM MPMS3 Superconducting Quantum Interference Device (SQUID) from Quantum Design. This system allows both conventional DC and VSM-type measurements. The hysteresis loops were measured at 2 K while the field switched from −4 T to 4 T. For zero field cooling purposes the magnet was quenched to minimize the residual magnetic field. Depending on sample and measurement type the effective sensitivity was in the range of 10^{-8}–10^{-9} emu.

Surface photovoltage spectroscopy (SPS) measurements were performed using a vibrating gold mesh Kelvin probe (3 mm diameter, Delta PHI Besocke) mounted 1 mm above the film samples. Samples were placed inside a home-built vacuum chamber ($p \approx 10^{-4}$ mbar by a *Pfeiffer HiCube 80 Eco* turbo pump station). Monochromatic radiation was provided by a 150 W Xe lamp using an Oriel Cornerstone 130 monochromator ($I_0 \approx 1$ mW·cm^{-2}). It was not compensated for the variable light intensity of the Xe lamp. A signal drift in the spectra was corrected by subtracting a dark background from the raw data. All reported contact potential difference (*CPD*) values were corrected by the *CPD* value in the dark. Effective bandgaps were obtained from the major photovoltage signals of the spectra using the tangent method. Charge separation reversibility was examined with light on/off scans at 2.48 eV monochromatic illumination.

Conflicts of interest

All authors declare no conflicts of interest. All authors approved the submission of the manuscript.

Author Contributions

C.B. developed and synthesized the oxide precursors and perovskite-type oxynitrides, performed and analyzed *in situ* ammonolysis, PXRD, DRS and TGA. M.W. and A.W. contributed to the discussion of the analysis. A.D. and F.O. performed and interpreted the SPS results with input from C.B. and M.W. M.C. and M.W. measured together HR-PXRD whereas the data was refined by C.B. C.B., M.W., S.Y., and M.C. further interpreted the resulted Rietveld refinements from HR-PXRD and ND. G.R. and C.B. interpreted together the XPS data. E.S.C. and C.B.

elaborated collectively the XANES data measured by E.S.C. C.B. and E.G. interpreted together the from E.G. and C.B. measured SQUID data. H.Z. performed and analyzed the DFT calculations with input from C.B. and M.W. C.B. wrote the paper. A.W. provided the research topic and contributions to the conclusions.

Acknowledgements

References

1   G. Zhang, G. Liu, L. Wang and J. T. S. Irvine, *Chem. Soc. Rev.*, 2016, 45, 5951–5984.

2   S. G. Ebbinghaus, H. P. Abicht, R. Dronskowski, T. Müller, A. Reller and A. Weidenkaff, *Prog. Solid State Chem.*, 2009, **37**, 173–205.

3   X. Chen, S. Shen, L. Guo and S. S. Mao, *Chem. Rev.*, 2010, **110**, 6503–6570.

4   J. Seo, T. Hisatomi, M. Nakabayashi, N. Shibata, T. Minegishi, M. Katayama and K. Domen, *Adv. Energy Mater.*, 2018, **8**, 1800094.

5   Y. K. Gaudy, S. Dilger, S. Landsmann, U. Aschauer, S. Pokrant and S. Haussener, *J. Mater. Chem. A*, 2018, **6**, 17337–17352.

6   J. Seo, M. Nakabayashi, T. Hisatomi, N. Shibata, T. Minegishi, M. Katayama and K. Domen, *J. Mater. Chem. A*, 2019, **7**, 493–502.

7   X. Sun, F. Wu, G. Liu and X. Xu, *J. Mater. Chem. A*, 2018, **6**, 20760–20768.

8   S. Ninova and U. Aschauer, *J. Mater. Chem. A*, 2017, **5**, 11040–11046.

9   M. Kodera, H. Urabe, M. Katayama, T. Hisatomi, T. Minegishi and K. Domen, *J. Mater. Chem. A*, 2016, **4**, 7658–7664.

10   M. Hojamberdiev, E. Zahedi, E. Nurlaela, K. Kawashima, K. Yubuta, M. Nakayama, H. Wagata, T. Minegishi, K. Domen and K. Teshima, *J. Mater. Chem. A*, 2016, **4**, 12807–12817.

11   A. E. Maegli, E. H. Otal, T. Hisatomi, S. Yoon, C. M. Leroy, N. Schäuble, Y. Lu, M. Grätzel and A. Weidenkaff, *Energy Procedia*, 2011, **22**, 61–66.

12   M. Hojamberdiev, M. F. Bekheet, J. N. Hart, J. J. M. Vequizo, A. Yamakata, K. Yubuta, A. Gurlo, M. Hasegawa, K. Domen and K. Teshima, *Phys. Chem. Chem. Phys.*, 2017, **19**, 22210–22220.

13   R. Marchand, F. Pors and Y. Laurent, *Ann. Chim. Fr.*, 1991, **16**, 553–560.

14   C. Bubeck, M. Widenmeyer, G. Richter, M. Coduri, E. Goering, S. Yoon and A. Weidenkaff, *Commun. Chem.*, 2019, **2**, 134.

15   C. Pan, T. Takata, K. Kumamoto, S. S. Khine Ma, K. Ueda, T. Minegishi, M. Nakabayashi, T. Matsumoto, N. Shibata, Y. Ikuhara and K. Domen, *J. Mater. Chem. A*, 2016, **4**, 4544–4552.

16   H. Kato, K. Ueda, M. Kobayashi and M. Kakihana, *J. Mater. Chem. A*, 2015, **3**, 11824–11829.

17   S. Ninova and U. Aschauer, *J. Mater. Chem. A*, 2019, **7**, 2129–2134.

18   J. Zhou, C. Zhou, Z. Shi, Z. Xu, S. Yan and Z. Zou, *J. Mater. Chem. A*, 2018, **6**, 7706–7713.

19   Y. Liu, W. Wang, X. Xu, J. P. Marcel Veder and Z. Shao, *J. Mater. Chem. A*, 2019, **7**, 7280–7300.

20   K. Maeda, H. Terashima, K. Kase, M. Higashi, M. Tabata and K. Domen, *Bull. Chem. Soc. Jpn.*, 2008, **81**, 927–937.

21   K. Maeda, M. Higashi, D. Lu, R. Abe and K. Domen, *J. Am. Chem. Soc.*, 2010, **132**, 5858–5868.

22   M. Hojamberdiev, M. F. Bekheet, J. N. Hart, J. J. M. Vequizo, A. Yamakata, K. Yubuta, A. Gurlo, M. Hasegawa, K. Domen and K. Teshima, *Phys. Chem. Chem. Phys.*, 2017, **19**, 22210–22220.

23   M. Liu, W. You, Z. Lei, T. Takata, K. Domen and C. Li, *Chinese J. Catal.*, 2006, **27**, 556–558.

24   L. Zhang, Y. Song, J. Feng, T. Fang, Y. Zhong, Z. Li and Z. Zou, *Int. J. Hydrogen Energy*, 2014, **39**, 7697–7704.

25   S. K. Suram, S. W. Fackler, L. Zhou, A. T. N'Diaye, W. S. Drisdell, J. Yano and J. M. Gregoire, *ACS Comb. Sci.*, 2018, **20**, 26–34.

26   I. E. Castelli, J. M. García-Lastra, F. Hüser, K. S. Thygesen and K. W. Jacobsen, *New J. Phys.*, 2013, **15**, 105026 (14pp).

27   I. E. Castelli, D. D. Landis, K. S. Thygesen, S. Dahl, I. Chorkendorff, T. F. Jaramillo and K. W. Jacobsen, *Energy Environ. Sci.*, 2012, **5**, 9034–9043.

28   I. E. Castelli, K. S. Thygesen and K. W. Jacobsen, *J. Mater. Chem. A*, 2015, **3**, 12343–12349.

29   R. Vadapoo, M. Ahart, M. Somayazulu, N. Holtgrewe, Y. Meng, Z. Konopkova, R. J. Hemley and R. E. Cohen, *Phys. Rev. B*, 2017, **95**, 1–5.

30   W. Si, Z. P. Tehrani, F. Haydous, N. Marzari, I. E. Castelli, D. Pergolesi and T. Lippert, *J. Phys. Chem. C*, 2019, **123**, 26211–26217.

31   M. Widenmeyer, C. Peng, A. Baki, W. Xie, R. Niewa and A. Weidenkaff, in *Solid State Sciences*, 2016, vol. 54, pp. 7–16.

32   W. Li, E. Ionescu, R. Riedel and A. Gurlo, *J. Mater. Chem. A*, 2013, **1**, 12239–12245.

33   K. S. Exner, *ChemElectroChem*, 2018, **5**, 3243–3248.

34   R. Parsons, *Trans. Faraday Soc.*, 1958, **54**, 1053–1063.

35   M. Pichler, J. Szlachetko, I. E. Castelli, N. Marzari, M. Döbeli, A. Wokaun, D. Pergolesi and T. Lippert, *ChemSusChem*, 2017, **10**, 2099–2106.

36   P. Maillard, F. Tessier, E. Orhan, F. Cheviré and R. Marchand, *Chem. Mater.*, 2005, **17**, 152–156.

37   H. Schilling, H. Wolff, R. Dronskowski and M. Lerch, *Zeitschrift fur Naturforsch. - Sect. B J. Chem. Sci.*, 2006, **61**, 660–664.

38   H. Wolff, H. Schilling, M. Lerch and R. Dronskowski, *J. Solid State Chem.*, 2006, **179**, 2265–2270.

39   P. Maillard, O. Merdrignac-Conanec and F. Tessier, *Mater. Res. Bull.*, 2008, **43**, 30–37.

40 M. Zhong, T. Hisatomi, Y. Sasaki, S. Suzuki, K. Teshima, M. Nakabayashi, N. Shibata, H. Nishiyama, M. Katayama, T. Yamada and K. Domen, *Angew. Chemie Int. Ed.*, 2017, **56**, 4739–4743.

41 J. Su, T. Minegishi, Y. Kageshima, H. Kobayashi, T. Hisatomi, T. Higashi, M. Katayama and K. Domen, *J. Phys. Chem. Lett.*, 2017, **8**, 5712–5717.

42 T. Hisatomi, J. Kubota and K. Domen, *Chem. Soc. Rev.*, 2014, **43**, 7520–7535.

43 L. Kronik and Y. Shapira, *Surf. Sci. Rep.*, 1999, **37**, 1–206.

44 X. Ma, X. Cui, Z. Zhao, M. A. Melo, E. J. Roberts and F. E. Osterloh, *J. Mater. Chem. A*, 2018, **6**, 5774–5781.

45 M. Rodríguez-Pérez, E. J. Canto-Aguilar, R. García-Rodríguez, A. T. De Denko, G. Oskam and F. E. Osterloh, *J. Phys. Chem. C*, 2018, **122**, 2582–2588.

46 M. A. Melo, Z. Wu, B. A. Nail, A. T. De Denko, A. F. Nogueira and F. E. Osterloh, *Nano Lett.*, 2018, **18**, 805–810.

47 Z. Wu, Z. Zhao, G. Cheung, R. M. Doughty, A. R. Ballestas-Barrientos, B. Hirmez, R. Han, T. Maschmeyer and F. E. Osterloh, *J. Electrochem. Soc.*, 2019, **166**, H3014–H3019.

48 S. H. Porter, Z. Huang and P. M. Woodward, *Cryst. Growth Des.*, 2014, **14**, 117–125.

49 P. Hartman and H. K. Chan, *Pharm. Res. An Off. J. Am. Assoc. Pharm. Sci.*, 1993, **10**, 1052–1058.

50 G. Kortüm, W. Braun and G. Herzog, *Angew. Chemie Int. Ed. English*, 1963, **2**, 333–341.

51 P. Thiel, S. Populoh, S. Yoon, G. Saucke, K. Rubenis and A. Weidenkaff, *J. Phys. Chem. C*, 2015, **119**, 21860–21867.

52 N. Vonrüti and U. Aschauer, *Phys. Rev. Mater.*, 2018, **2**, 105401.

53 R. F. Berger, C. J. Fennie and J. B. Neaton, *Phys. Rev. Lett.*, 2011, **107**, 1–5.

54 Z. C. Zhao, C. L. Yang, Q. T. Meng, M. S. Wang and X. G. Ma, *Appl. Phys. A Mater. Sci. Process.*, 2019, 125.

55 D. Briggs and J. T. Grant, *Surface Analysis by Auger and X-ray Photoelectron Spectroscopy*, IM Publications, 2003.

56 C. Nordling, *Angew. Chemie*, 1972, **4**, 144–153.

57 G. S. Henderson, F. M. F. De Groot and B. J. A. Moulton, *Rev. Mineral. Geochemistry*, 2014, **78**, 75–138.

58 T. Siegrist, R. J. Cava and J. J. Krajewski, *Mater. Res. Bull.*, 1997, **32**, 881–887.

59 J. E. Penner-Hahn, *Encycl. Life Sci.*, 2005, 2–5.

60 A. O. Ibidunni, R. L. Masaitis, R. L. Opila, A. J. Davenport, H. S. Isaacs and J. A. Taylor, *Surf. Interface Anal.*, 1993, **20**, 559–564.

61 B. Poumellec, J. F. Marucco and E. Touzelin, *Phys. status solidi*, 1986, **137**, 519–531.

62 J. M. D. Coey, *Solid State Sci.*, 2005, **7**, 660–667.

63 Y. C. Chen, E. Goering, L. Jeurgens, Z. Wang, F. Phillipp, J. Baier, T. Tietze and G. Schütz, *Appl. Phys. Lett.*, 2013, **103**, 162405.

64 T. Tietze, P. Audehm, Y. C. Chen, G. Schütz, B. B. Straumal, S. G. Protasova, A. A. Mazilkin, P. B. Straumal, T. Prokscha, H. Luetkens, Z. Salman, A. Suter, B. Baretzky, K. Fink, W. Wenzel, D. Danilov and E. Goering, *Sci. Rep.*, 2015, **5**, 5 : 8871.

65 B. D. Cullity and C. D. Graham, *Introduction to magnetic materials*, John Wiley & Sons Inc., 2nd edn., 2008.

66 D. Tatar and B. Düzgün, *Pramana - J. Phys.*, 2012, **79**, 137–150.

67 J. Jia, A. Takaya, T. Yonezawa, K. Yamasaki, H. Nakazawa and Y. Shigesato, *J. Appl. Phys.* 125, 245303.

68 H. Liu, X. Shi, F. Xu, L. Zhang, W. Zhang, L. Chen, Q. Li, C. Uher, T. Day and G. Snyder Jeffrey, *Nat. Mater.*, 2012, **11**, 422–425.

69 T. L. Shelton, N. Harvey, J. Wang and F. E. Osterloh, *Appl. Catal. A Gen.*, 2016, **521**, 168–173.

70 T. Takata and K. Domen, *J. Phys. Chem. C*, 2009, **113**, 19386–19388.

71 M. Widenmeyer, T. Kohler, M. Samolis, A. T. D. Denko, X. Xiao, W. Xie, F. E. Osterloh and A. Weidenkaff, *Zeitschrift fur Phys. Chemie*, 2020, 1–23.

72 Y. Wang, S. Jin, G. Pan, Z. Li, L. Chen, G. Liu and X. Xu, *J. Mater. Chem. A*, 2019, **7**, 5702–5711.

73 K. Koepernik and H. Eschrig, *Phys. Rev. B - Condens. Matter Mater. Phys.*, 1999, **59**, 1743–1757.

74 Please also see http://www.fplo.de for the documentation of the code.

75 J. P. Perdew, K. Burke and M. Ernzerhof, *Phys. Rev. Lett.*, 1996, **77**, 3865–3868.

76 H. M. Rietveld, *Acta Crystallogr.*, 1967, **22**, 151–152.

77 H. M. Rietveld, *J. Appl. Crystallogr.*, 1969, **2**, 65–71.

78 J. Rodriguez-Carvajal, *2012*.

79 M. Hoelzel, A. Senyshyn and O. Dolotko, *J. large-scale Res. Facil. JLSRF*, 2015, **1**, 5.

80 S. Brunauer, P. H. Emmett and E. Teller, *J. Am. Chem. Soc.*, 1938, **60**, 309–319.

81 G. R. Castro, *J. Synchrotron Radiat.*, 1998, **5**, 657–660.

82 B. Ravel and M. Newville, *J. Synchrotron Radiat.*, 2005, **12**, 537–541.